



Article

Hexagonal and Monoclinic Phases of $\text{La}_2\text{O}_2\text{CO}_3$ Nanoparticles and Their Phase-Related CO_2 Behavior

Hongyan Yu ^{1,2}, Kaiming Jiang ^{1,2}, Sung Gu Kang ¹, Yong Men ² and Eun Woo Shin ^{1,*}

¹ School of Chemical Engineering, University of Ulsan, Daehakro 93, Nam-gu, Ulsan 44610, Korea; yuyubobo0908@163.com (H.Y.); hg041111138@163.com (K.J.); sgkang@ulsan.ac.kr (S.G.K.)

² College of Chemistry and Chemical Engineering, Shanghai University of Engineering Science, Shanghai 201620, China; men@sues.edu.cn

* Correspondence: ewshin@ulsan.ac.kr

Received: 28 September 2020; Accepted: 15 October 2020; Published: 19 October 2020



Abstract: In this study, we prepared hexagonal and monoclinic phases of $\text{La}_2\text{O}_2\text{CO}_3$ nanoparticles by different wet preparation methods and investigated their phase-related CO_2 behavior through field-emission scanning microscopy, high-resolution transmission electron microscopy, Fourier transform infrared, thermogravimetric analysis, CO_2 -temperature programmed desorption, and linear sweeping voltammetry of CO_2 electrochemical reduction. The monoclinic $\text{La}_2\text{O}_2\text{CO}_3$ phase was synthesized by a conventional precipitation method via $\text{La}(\text{OH})\text{CO}_3$ when the precipitation time was longer than 12 h. In contrast, the hydrothermal method produced only the hexagonal $\text{La}_2\text{O}_2\text{CO}_3$ phase, irrespective of the hydrothermal reaction time. The $\text{La}(\text{OH})_3$ phase was determined to be the initial phase in both preparation methods. During the precipitation, the $\text{La}(\text{OH})_3$ phase was transformed into $\text{La}(\text{OH})\text{CO}_3$ owing to the continuous supply of CO_2 from air whereas the hydrothermal method of a closed system crystallized only the $\text{La}(\text{OH})_3$ phase. Based on the CO_2 -temperature programmed desorption and thermogravimetric analysis, the hexagonal $\text{La}_2\text{O}_2\text{CO}_3$ nanoparticles (HL-12h) showed a higher surface CO_2 adsorption and thermal stability than those of the monoclinic $\text{La}_2\text{O}_2\text{CO}_3$ (PL-12h). The crystalline structures of both $\text{La}_2\text{O}_2\text{CO}_3$ phases predicted by the density functional theory calculation explained the difference in the CO_2 behavior on each phase. Consequently, HL-12h showed a higher current density and a more positive onset potential than PL-12h in CO_2 electrochemical reduction.

Keywords: monoclinic; hexagonal; $\text{La}_2\text{O}_2\text{CO}_3$ phase; CO_2 behavior; precipitation method; hydrothermal method

1. Introduction

Recently, the synthesis of nanomaterials with controllable morphologies and phases has attracted considerable attention in the fields of materials science and inorganic chemistry because the physicochemical and structural properties of the nanomaterials strongly correlate with the types of crystal structures as well as the morphologies of nanoparticles [1–6]. The unique properties of nanomaterials can be properly tuned by controlling various factors, which results in potential applications of nanomaterials in catalysis, biological labeling, sensing, and optics [1,7–9]. Among the methods for synthesizing nanomaterials, wet chemical processes have been considered as the most effective and convenient approaches for the controllable phases of ceramic materials [10].

Lanthana (La_2O_3) has been widely used as a promoter or support in heterogeneous catalysis [11–13]. The basicity of La_2O_3 readily induces the adsorption of CO_2 to form the lanthanum oxycarbonate ($\text{La}_2\text{O}_2\text{CO}_3$) phase, which is an important species in the La_2O_3 -containing catalytic reaction [4,13–16]. The crystalline structures of $\text{La}_2\text{O}_2\text{CO}_3$ can be divided into three types of different polymorphs:

a tetragonal $\text{La}_2\text{O}_2\text{CO}_3$ (type I), a monoclinic $\text{La}_2\text{O}_2\text{CO}_3$ (type Ia), and a hexagonal $\text{La}_2\text{O}_2\text{CO}_3$ (type II) [16–18]. The hexagonal type II $\text{La}_2\text{O}_2\text{CO}_3$ has a higher chemical stability to water and carbon dioxide than the monoclinic type Ia [4,19,20]. In addition, the different crystalline structures of the $\text{La}_2\text{O}_2\text{CO}_3$ phases affect the interaction between $\text{La}_2\text{O}_2\text{CO}_3$ and ZnO in the $\text{La}_2\text{O}_2\text{CO}_3/\text{ZnO}$ composite materials as well as the catalytic behavior of the composite materials on glycerol carbonation with CO_2 [4,21]. Meanwhile, the monoclinic type Ia $\text{La}_2\text{O}_2\text{CO}_3$ phase closely resembles the crystalline structure of lanthanum (La) oxysalts (e.g., oxysilicates, oxyhalides, and oxysulfates), whereas the hexagonal type II one is similar to A-type La sesquioxides. Thus, the type Ia $\text{La}_2\text{O}_2\text{CO}_3$ phase has been readily prepared by the thermal decomposition of La compounds (e.g., oxalates and acetates); however, it is difficult to prepare type II $\text{La}_2\text{O}_2\text{CO}_3$ in a single phase by the conventional wet preparation methods [20]. Accordingly, it is necessary to investigate i) the preparation conditions used to form type Ia and type II $\text{La}_2\text{O}_2\text{CO}_3$ phases in the conventional methods and ii) the CO_2 behavior on the $\text{La}_2\text{O}_2\text{CO}_3$ structures, which is an essential step in the CO_2 -involving catalytic reactions, as well as the formation of the different $\text{La}_2\text{O}_2\text{CO}_3$ phases.

In this study, we prepared the nanoparticles with type Ia and type II $\text{La}_2\text{O}_2\text{CO}_3$ crystal structures by conventional wet preparation methods and investigated the formation of different $\text{La}_2\text{O}_2\text{CO}_3$ phases with Fourier transform infrared (FT-IR), X-ray diffraction (XRD), field-emission scanning electron microscopy (FE-SEM), and high-resolution transmission electron microscopy (HR-TEM). Furthermore, the CO_2 behavior on the different $\text{La}_2\text{O}_2\text{CO}_3$ crystal structures was observed by CO_2 -temperature programmed desorption (TPD), thermogravimetric analysis (TGA), and linear sweeping voltammetry (LSV) of CO_2 electrochemical reduction. The superior CO_2 behavior of the hexagonal $\text{La}_2\text{O}_2\text{CO}_3$ phase to the monoclinic phase was additionally explained by the crystalline structures of both $\text{La}_2\text{O}_2\text{CO}_3$ phases, which was predicted by the density functional theory (DFT) calculation.

2. Materials and Methods

2.1. Materials

A total of 1.00 g of $\text{La}(\text{NO}_3)_3 \cdot 6\text{H}_2\text{O}$ was added to 50.0 mL of deionized water, and the resultant solution was vigorously stirred to ensure complete dissolution. The pH of the solution was adjusted to 12 with a 10 wt% NaOH solution, which yielded a white precipitate after the mixture was stirred for approximately 10 min. The sample was continuously stirred for another 6, 12, or 24 h, and the obtained product was centrifuged. The separated precipitate was washed with distilled water and ethanol and then dried at 80 °C for 12 h, followed by the calcination step at 500 °C for 2 h. Depending on the precipitation time, the solid samples prepared by the precipitation method were denoted as PL-*x*h (*x* = 6, 12, or 24), where *x* represents the precipitation time.

For the hydrothermal method, the procedure was almost the same as that in the precipitation method, except using an autoclave for the hydrothermal treatment. The pH-adjusted solution containing the La precursor was transferred to an autoclave (200 mL), heated to 160 °C, and maintained at this temperature for 6, 12, or 24 h. The obtained product was centrifuged, and the remained steps were also the same as those in the precipitation method. The $\text{La}_2\text{O}_2\text{CO}_3$ samples synthesized by the hydrothermal method were designated as HL-*y*h (*y* = 6, 12, or 24), where *y* represents the hydrothermal treatment time.

2.2. Characterizations

The morphologies of the samples were observed by a field-emission scanning electron microscope (JEOL, JSM-600F, Tokyo, Japan) instrument equipped with an energy-dispersive spectrometer. HR-TEM images were obtained using a JEOL JEM-2100F instrument (JEOL Ltd., Tokyo, Japan). The samples were prepared by suspending and grinding in an ethanol solution whose drops were placed on a carbon-film-coated copper grid. XRD patterns were measured at room temperature on a Rigaku D/MAX-2200 powder X-ray diffractometer (Rigaku Corporation, Tokyo, Japan) using a $\text{Cu K}\alpha$ radiation

source ($\lambda = 0.15418$ nm). The X-ray tube was operated at 35 kV and 20 mA, and the 2θ angle was scanned from 10° to 90° (with a step of 0.02°) at a speed of $2^\circ/\text{min}$. The FT-IR spectra of the samples were collected for the KBr powder-pressed pellets on a Nicolet 380 FT-IR spectrophotometer (Thermo Fisher Scientific, Waltham, MA, USA) under ambient conditions.

The CO_2 -TPD experiments were conducted in a quartz flow reactor. The calcined samples were preheated from room temperature up to 600°C (with a ramping rate of $15^\circ\text{C}/\text{min}$) for 1 h under He flow (100 mL/min). The CO_2 gas (10 vol.% CO_2/He) was fed into the reactor with a flow rate of 30 mL/min at 50°C for CO_2 adsorption before conducting the CO_2 -TPD measurements. Finally, the temperature was increased from 50 to 600°C at the ramping rate of $1.5^\circ\text{C}/\text{min}$ in He flow (30 mL/min). The weight loss in the samples was determined by a thermogravimetric analyzer (TA Instruments Q50, New Castle, DE, USA). A total of 20 mg of the samples was charged into the sample pan and heated to 1000°C at a rate of $5^\circ\text{C}/\text{min}$ in air flow. The CO_2 electrochemical reduction was carried out via the LSV measurement with an Ag/AgCl electrode as a reference electrode and Pt wire as a counter electrode. The working electrode was prepared by dispersing 10 mg of the samples in a mixture of 2 mL of alcohol and 100 μL of 5% Nafion and then pipetting 10 μL of suspension on the GCE (0.07065 cm^2). The working electrode was tested 20 times at a scan rate of 20 mV/s. The electrolyte was 0.1 M NaHCO_3 saturated with CO_2 . Before each experiment, high-purity CO_2 gas was bubbled at a flow rate of 30 mL/min for 30 min to remove all oxygen from the electrolyte. The gases in the measurement were analyzed by a GC instrument.

Using the Vienna Ab initio Simulation Package (VASP) [22,23], DFT calculations were conducted along with the GGA-PBE (Perdew-Burke-Ernzerhof) functional [24]. The cutoff energy of 600 eV was chosen in our calculations. The criteria of convergence of energies and forces for geometry optimization were 10^{-4} eV and 10^{-2} eV/ \AA , respectively. For the calculation of disordered hexagonal $\text{La}_2\text{O}_2\text{CO}_3$, the lowest energy configuration among the other randomly selected 50 structures was used. The Monkhorst-Pack k -point meshes of $3 \times 5 \times 2$ and $9 \times 9 \times 3$ were used for the geometry optimization of monoclinic and hexagonal phase of $\text{La}_2\text{O}_2\text{CO}_3$, respectively [25].

3. Results and Discussion

3.1. Synthesis of Monoclinic and Hexagonal $\text{La}_2\text{O}_2\text{CO}_3$ Nanoparticles

Figure 1 shows the XRD patterns of $\text{La}_2\text{O}_2\text{CO}_3$ nanoparticle materials prepared at each reaction time. The two types of $\text{La}_2\text{O}_2\text{CO}_3$ phases are primarily detected in the PL samples: the monoclinic type Ia and hexagonal type II $\text{La}_2\text{O}_2\text{CO}_3$ phases. For 6 h of precipitation (PL-6h), the characteristic XRD peaks in the hexagonal $\text{La}_2\text{O}_2\text{CO}_3$ crystal phase are clearly observed at $2\theta = 25.7, 30.2, 47.2,$ and 56.6° (JCPDS 37-0804) (Figure 1(Aa)) [1,4,20,21,26,27]. However, when the precipitation time is increased to 12 and 24 h, the characteristic XRD peaks in the monoclinic $\text{La}_2\text{O}_2\text{CO}_3$ phase clearly appear at $2\theta = 22.8, 29.3, 31.0, 39.9,$ and 44.4° with a C12/c1 space group (JCPDS 48-1113) (Figure 1(Ab,Ac)), which indicates the prevalence of the hexagonal $\text{La}_2\text{O}_2\text{CO}_3$ phase during the initial precipitation time, followed by the transformation into the monoclinic $\text{La}_2\text{O}_2\text{CO}_3$ phase after 12 h of precipitation. In contrast, the HL samples show the XRD patterns that contain the characteristic peaks in only the hexagonal type II $\text{La}_2\text{O}_2\text{CO}_3$ phase, regardless of the reaction time during the hydrothermal preparation, which demonstrates that there is no change in the $\text{La}_2\text{O}_2\text{CO}_3$ phase during the preparation process (Figure 1(Ba–Bc)).

The FT-IR spectra of the PL and HL samples also confirm the formation of each $\text{La}_2\text{O}_2\text{CO}_3$ crystal phase depending on the preparation methods, as shown in Figure 2. According to the assignments of typical FT-IR bands for carbonates in the $\text{La}_2\text{O}_2\text{CO}_3$ phases, the bands at 745, 855, 1066, and 1518 cm^{-1} are interpreted as CO_3^{2-} vibrations related to the $\text{La}_2\text{O}_2\text{CO}_3$ phase [4,6,21,27]. The three-fold splitting bands at approximately 845 cm^{-1} (ν_2) and a strong band at 1367 cm^{-1} (ν_3) are assigned to the unique carbonate vibrational mode for the monoclinic type Ia $\text{La}_2\text{O}_2\text{CO}_3$ phase. The FT-IR spectra in Figure 2b,c of only the PL-12h and PL-24h samples show the characteristic bands (ν_2 and ν_3) of type-Ia

$\text{La}_2\text{O}_2\text{CO}_3$, whereas the FT-IR spectra of the other samples show the typical bands of the $\text{La}_2\text{O}_2\text{CO}_3$ phase, which further confirms that the formation of the type Ia and II $\text{La}_2\text{O}_2\text{CO}_3$ phases depends on the preparation conditions. In the precipitation method, the monoclinic type Ia $\text{La}_2\text{O}_2\text{CO}_3$ phase is mainly formed when the precipitation time is longer than 12 h, whereas the hydrothermal method produces only the hexagonal type II $\text{La}_2\text{O}_2\text{CO}_3$ phase. This is consistent with the XRD results in this study.

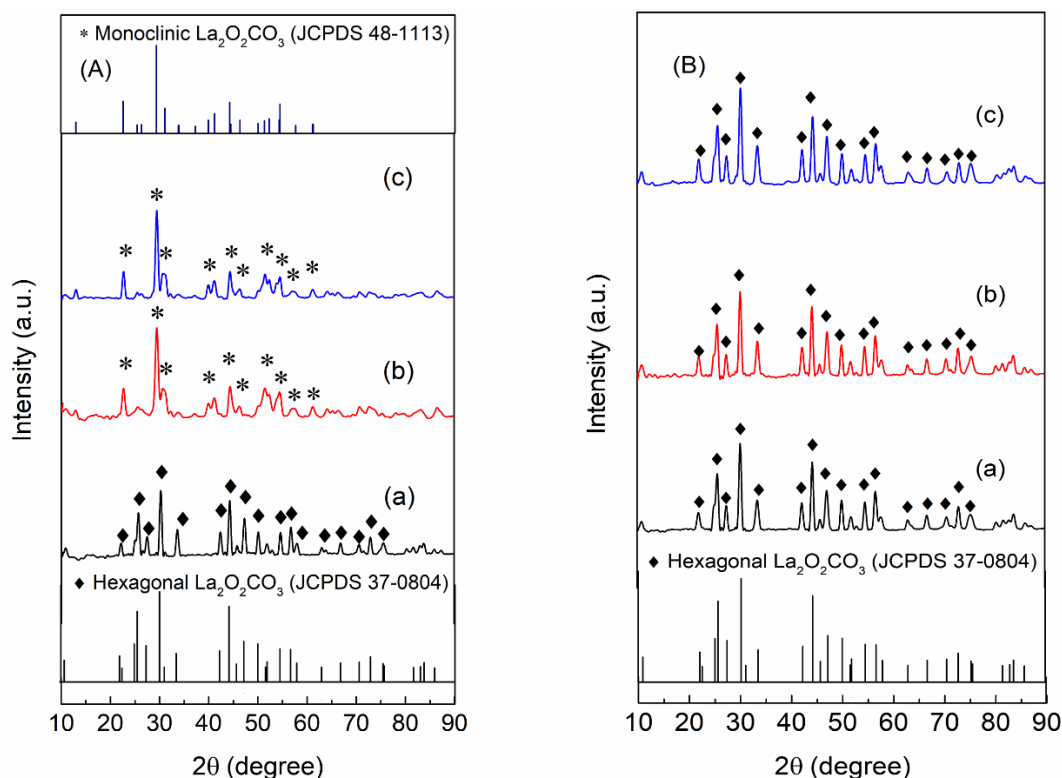


Figure 1. XRD patterns of A(a–c) PL-6h, PL-12h, and PL-24h and B(a–c) HL-6h, HL-12h, and HL-24h.

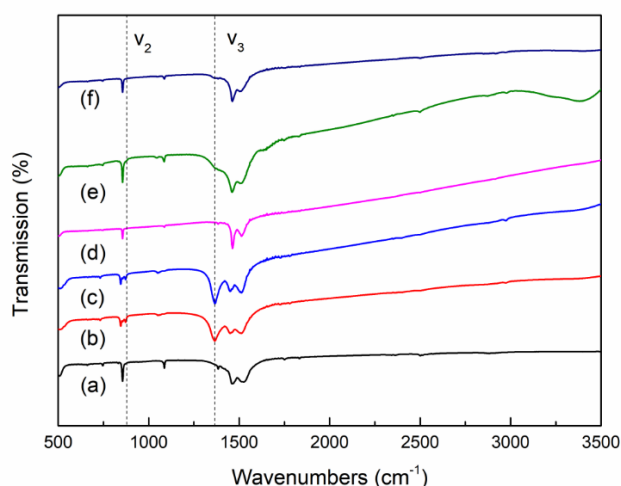


Figure 2. FT-IR spectra of (a) PL-6h, (b) PL-12h, (c) PL-24h, (d) HL-6h, (e) HL-12h, and (f) HL-24h.

Moreover, TEM measurements also provide additional evidence for the existence of the monoclinic and hexagonal $\text{La}_2\text{O}_2\text{CO}_3$ phases in the samples. Figure 3a–c shows the TEM images and fast Fourier transform patterns of PL-6h, PL-12h, and HL-12h. The (207) plane of the monoclinic type Ia $\text{La}_2\text{O}_2\text{CO}_3$ phase is detected in the PL-12h sample, whereas the (260) plane of the hexagonal type II $\text{La}_2\text{O}_2\text{CO}_3$

phase is observed in the HL-12h sample. Similarly, the PL-6h sample shows the (004) plane of the type II $\text{La}_2\text{O}_2\text{CO}_3$ phase, which is in good agreement with the XRD and FT-IR data. However, the morphological structures of PL-12h, HL-12h, and PL-6h samples are similar, as shown by the FE-SEM images; the aggregates of nanoparticles have different sizes: smaller than 10 nm for PL-12h, 10–30 nm for HL-12h, and 30–60 nm for PL-6h (Figure 3d–f).

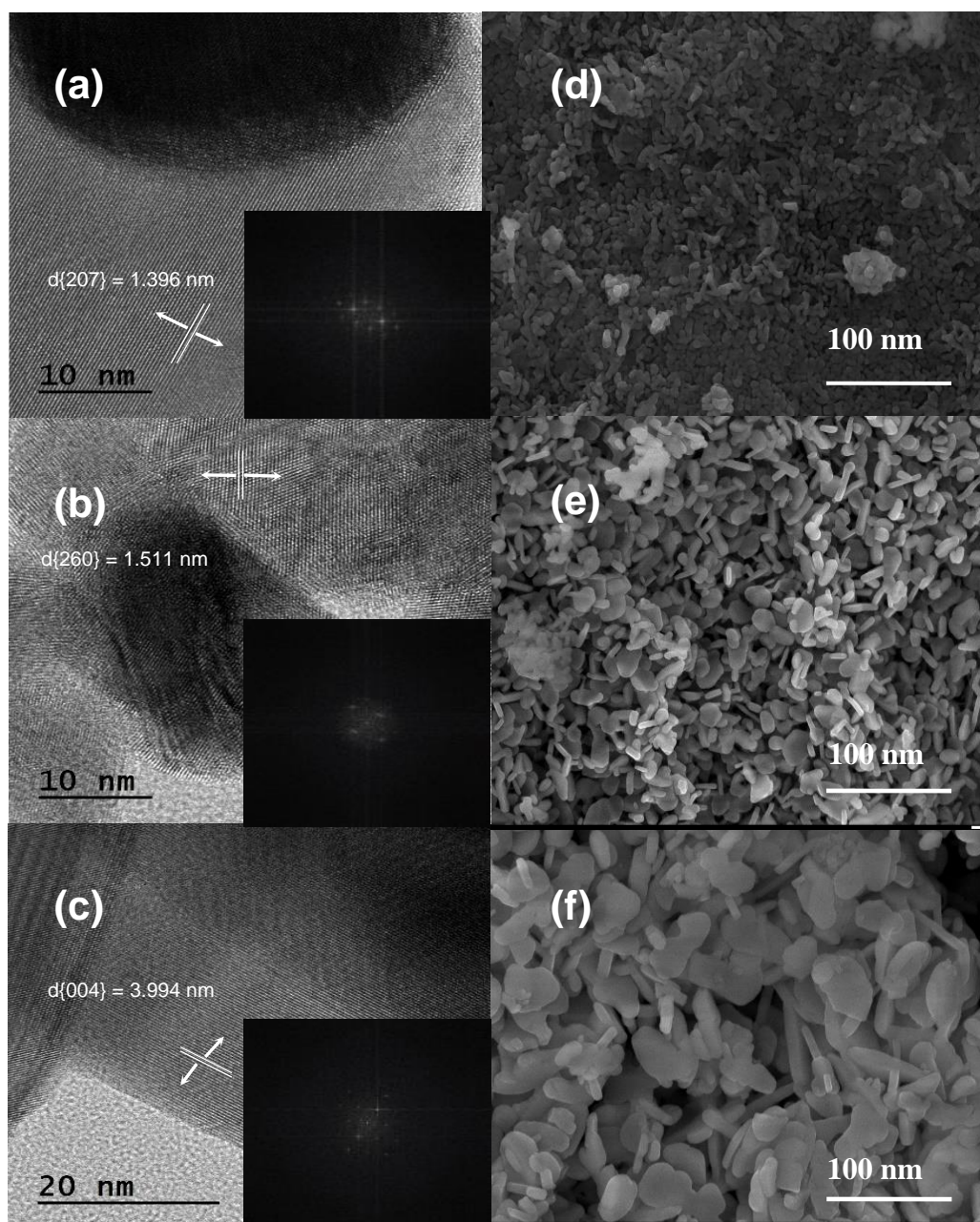


Figure 3. High-resolution transmission electron microscopy (HR-TEM) images of (a–c) PL-12h, HL-12h, and PL-6h, and FE-SEM images of (d–f) PL-12h, HL-12h, and PL-6h. The insets of (a–c) show their fast Fourier transform patterns.

To further understand the formation mechanism of the monoclinic and hexagonal $\text{La}_2\text{O}_2\text{CO}_3$ phases, uncalcined samples after precipitation or hydrothermal treatment were investigated. The XRD and FT-IR measurements indicate that different chemical products are also produced depending on the preparation conditions (Figure 4). The XRD peaks in Figure 4(Aa–Ac), shown as circles, are indexed to

the pure hexagonal phase of $\text{La}(\text{OH})_3$ with a $P63/m(176)$ space group (JCPDS 36-1481) [1,6,12,21,26–28], which clearly shows that the initial $\text{La}(\text{OH})_3$ phase remains unchanged in the hydrothermal method. With an increase in the preparation time during the hydrothermal method, the crystallinity of the $\text{La}(\text{OH})_3$ structure becomes stronger with sharper XRD characteristic peaks. Meanwhile, in the precipitation method, the $\text{La}(\text{OH})_3$ phase is produced with a very low crystallinity for PL-6h (weak and broad characteristic XRD peaks in Figure 4(Ac)). However, when the precipitation time is increased up to 12 h, the characteristic XRD peaks assigned to the orthorhombic $\text{La}(\text{OH})\text{CO}_3$ structure (JCPDS 49-0981) appear with the disappearance of the XRD peaks in the $\text{La}(\text{OH})_3$ structure (Figure 4(Ad)) [9,29]. Therefore, in the precipitation method, the dominant phase evolves from $\text{La}(\text{OH})_3$ to $\text{La}(\text{OH})\text{CO}_3$, with an increase in the precipitation time. However, the initial $\text{La}(\text{OH})_3$ phase in the hydrothermal method is more crystallized during the hydrothermal treatment.

The FT-IR spectra of the uncalcined samples are monitored to confirm the existence of $\text{La}(\text{OH})_3$ and $\text{La}(\text{OH})\text{CO}_3$. First, the strong bands at 1438 and 1491 cm^{-1} shown in Figure 4(Bd) can be assigned to the bending vibrations of CO_3^{2-} , which confirms the presence of carbonate species in the intermediate [9]. A band at 3616 cm^{-1} and a broad band at 3410 cm^{-1} represent the O–H stretching mode in La-OH [6,9,27]. The bands at 850 and 1052 cm^{-1} correspond to the vibrational modes of carbon-related bonds, such as CH and CO, which remain before the calcination step. Thus, the FT-IR spectrum in Figure 4(Bd) clearly confirms the existence of $\text{La}(\text{OH})\text{CO}_3$ as an intermediate in the PL-12h sample, which is consistent with the XRD data shown in Figure 4A. For $\text{La}(\text{OH})_3$, the characteristic FT-IR bands for the O–H stretching and bending modes in La-OH are clearly observed at 3616 , 3410 , and 1640 cm^{-1} , as shown in Figure 4(Ba–Bc) [6,9,27]. Other bands at approximately 2800 – 3000 , 850 , and 1052 cm^{-1} can also be assigned to the vibrational modes of carbon-related bonds. Interestingly, for the samples in the precipitation method, the characteristic IR bands for CO_3^{2-} at approximately 1350 – 1500 cm^{-1} become sharp and strong with an increase in the reaction time (Figure 4(Bc,Bd)), whereas the characteristic IR band for OH at 3616 cm^{-1} is strongly intensified during the hydrothermal method (Figure 4(Ba,Bb)). Therefore, the precipitation method induces the transformation from $\text{La}(\text{OH})_3$ into $\text{La}(\text{OH})\text{CO}_3$ through the reaction with CO_2 . In the hydrothermal method, the crystallization of $\text{La}(\text{OH})_3$ goes further, which results in the high crystallinity of $\text{La}(\text{OH})_3$.

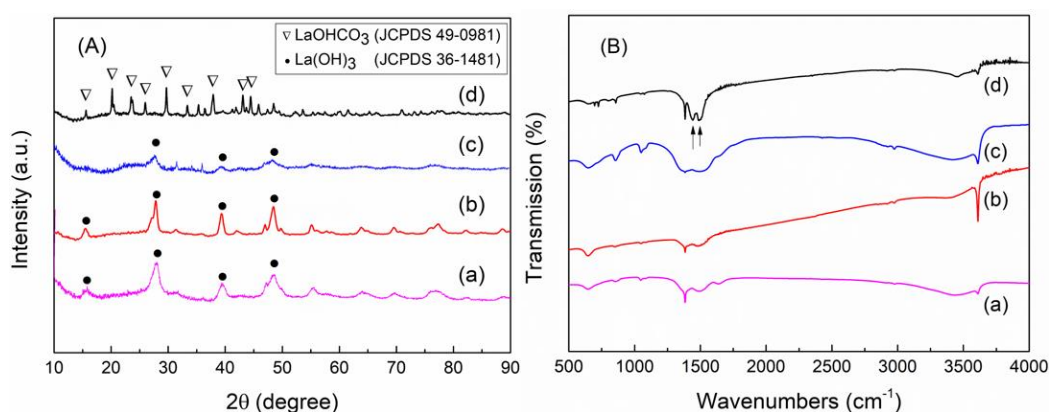


Figure 4. (A) XRD patterns and (B) FT-IR spectra of uncalcined samples. (a) HL-6h, (b) HL-12h, (c) PL-6h, and (d) PL-12h.

A critical difference between the two preparations is an open or closed reaction system, which is related to the supply of carbonate sources. For either the precipitation or hydrothermal method, the La precursor in the aqueous solution is dissociated into La cations and is then readily crystallized into the $\text{La}(\text{OH})_3$ phase, because the initial pH conditions are strongly basic (i.e., $\text{pH} = 12$). In the hydrothermal method, a Teflon-lined autoclave reactor is used as a closed reaction system. Because it is a closed system, there is no further transformation of the La intermediate, which only results in the strong crystallization of the $\text{La}(\text{OH})_3$ phase for the HL-12h and HL-24h samples. However, in the

precipitation method, the precipitation is carried out in an open beaker; thus, the carbonate source (i.e., CO_2 from the air) can be continuously dissolved into the aqueous solution. Therefore, the initial phase, $\text{La}(\text{OH})_3$, can be converted into the $\text{La}(\text{OH})\text{CO}_3$ phase by the reaction with CO_2 at a time longer than 12 h, even though the 6-h precipitation produces only a weakly crystallized $\text{La}(\text{OH})_3$. Under the continuous CO_2 supply condition, there is a transformation from $\text{La}(\text{OH})_3$ into $\text{La}(\text{OH})\text{CO}_3$. In the literature, it was reported that $\text{La}(\text{OH})_3$ changed into an La carbonate when it was exposed to air [6,27,28]. More importantly, the $\text{La}(\text{OH})\text{CO}_3$ phase is finally converted into the monoclinic type Ia $\text{La}_2\text{O}_2\text{CO}_3$ phase in the precipitation, while $\text{La}(\text{OH})_3$ is transformed into the hexagonal type II structure in the hydrothermal method. The sufficient supply of CO_2 into the aqueous solution produces the $\text{La}(\text{OH})\text{CO}_3$ that can be changed into the monoclinic $\text{La}_2\text{O}_2\text{CO}_3$ phase.

3.2. CO_2 Behavior on $\text{La}_2\text{O}_2\text{CO}_3$ Nanoparticles

To investigate the CO_2 behavior on each $\text{La}_2\text{O}_2\text{CO}_3$ phase, TGA, CO_2 -TPD and CV of CO_2 electrochemical reduction for PL-12h (monoclinic type Ia $\text{La}_2\text{O}_2\text{CO}_3$ phase) and HL-12h (hexagonal type II $\text{La}_2\text{O}_2\text{CO}_3$ phase) were conducted in this study. Figure 5A shows the derivative TGA (DTGA) profiles of PL-12h and HL-12h, where the decomposition peaks correspond to CO_2 gases that leave from the $\text{La}_2\text{O}_2\text{CO}_3$ phases. The weight loss due to the thermal decomposition occurs at 326 °C and in the temperature range of 770–800 °C. According to previous studies [4,30], the CO_2 peak, which appears during the decomposition of $\text{La}_2\text{O}_2\text{CO}_3$ above 600 °C, can be assigned to CO_2 gases leaving from the bulk structure of the $\text{La}_2\text{O}_2\text{CO}_3$ phases, which is then transformed into the La_2O_3 phase. The CO_2 decomposition from the bulk structure of the hexagonal $\text{La}_2\text{O}_2\text{CO}_3$ phase occurs at approximately 800 °C, which is higher than the temperature of CO_2 production during the decomposition of the bulk structure of the monoclinic $\text{La}_2\text{O}_2\text{CO}_3$ phase. This result shows that the thermal stability of the hexagonal $\text{La}_2\text{O}_2\text{CO}_3$ phase is higher than that of the monoclinic phase [21]. The weight loss at approximately 326 °C is assumed to be due to the release of CO_2 gas that is adsorbed on the surface of the $\text{La}_2\text{O}_2\text{CO}_3$ phase. The decomposition peak at approximately 326 °C has a much smaller intensity than that at 650 °C, which indicates that a much lower amount of CO_2 is adsorbed onto the surfaces of the $\text{La}_2\text{O}_2\text{CO}_3$ phase than that released from the bulk structure. Furthermore, based on each peak's intensity, shown in Figure 5A, the hexagonal type II $\text{La}_2\text{O}_2\text{CO}_3$ phase contains more CO_2 on the surface than that on the monoclinic type Ia phase.

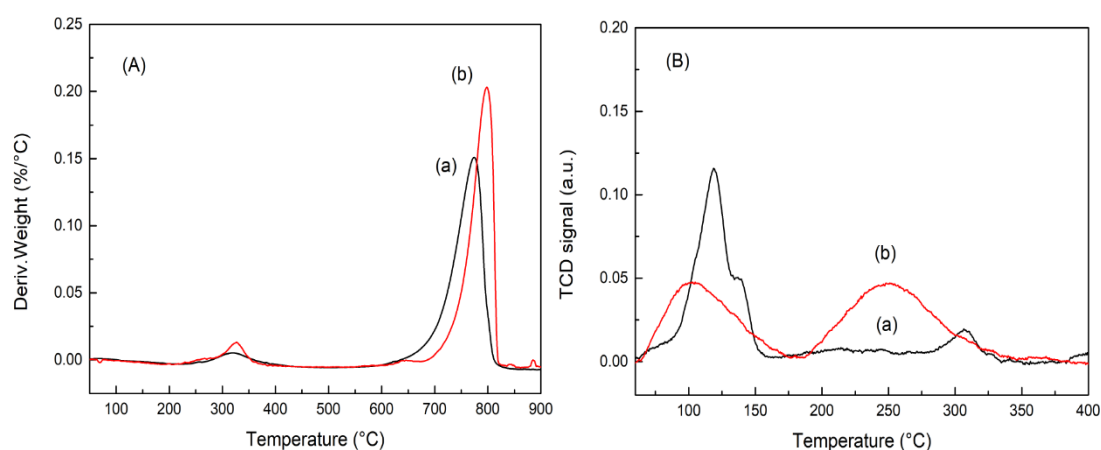


Figure 5. (A) Derivative thermogravimetric analysis (TGA) profiles and (B) CO_2 -temperature-programmed desorption (TPD) patterns of (a) PL-12h and (b) HL-12h.

To better understand the CO_2 adsorption ability on the surface of each $\text{La}_2\text{O}_2\text{CO}_3$ phase, the CO_2 -TPD profiles of PL-12h and HL-12h were acquired. Before conducting the CO_2 -TPD experiments, both samples were thermally treated at 600 °C for 1 h in He gas, and then CO_2 was introduced into the reactor at 50 °C to perform the CO_2 adsorption. Therefore, CO_2 can be assumed

to adsorb on the surface of $\text{La}_2\text{O}_2\text{CO}_3$ phases and then desorb from the adsorption surface sites, which demonstrates the CO_2 adsorption behavior on the monoclinic and hexagonal $\text{La}_2\text{O}_2\text{CO}_3$ phases. In Figure 5B, the CO_2 desorption peaks can be approximately categorized into three types. The peak at approximately 100 °C is related to a weak basic site, and the peaks in the range of 200–400 °C correspond to medium and strong basic sites [2,12,31,32]. The CO_2 adsorption modes on each basic site have been studied by a combination of FT-IR spectroscopy and CO_2 -TPD measurements [31,32]. Manoilova et al. [30] investigated the CO_2 adsorption onto La_2O_3 by IR spectroscopy, TPD, and DFT calculations. The DFT calculation for the CO_2 adsorption on La_2O_3 predicted that CO_2 gas adsorbed on the surface in the form of polydentate and monodentate species as a starting structure, and then La_2O_3 made a stable connection with polydentate and asymmetric CO_2 adsorptions at the saturated coverage. The CO_2 desorption peak at approximately 290 °C in the CO_2 -TPD profile of LaOCl was assigned to the decomposition of coupled bridged CO_2 adsorbate species [31]. On the basis of the results from the FT-IR and CO_2 -TPD measurements of Mg–Al basic oxides, Di Cosimo et al. [32] suggested that the three types of CO_2 adsorption modes (e.g., bicarbonate, bidentate carbonate, and unidentate carbonate) were low-strength, medium-strength, and high-strength basic sites, respectively. It was determined that bidentate and unidentate carbonates remained on the surface at approximately 300 °C; only unidentate carbonate was detected at 350 °C [32]. Therefore, in this study, the peak at 110 °C, peaks at approximately 240 °C, and shoulders at approximately 310 °C can be assigned to the desorption of CO_2 species adsorbed on weak, medium and strong basic sites, respectively. Figure 5B and Table 1 shows that the HL-12h sample has a higher combined intensity of medium and strong basic sites than PL-12h, which suggests that the hexagonal type II $\text{La}_2\text{O}_2\text{CO}_3$ phase provides more CO_2 adsorption sites on the surface. This observation is in good agreement with the TGA results shown in Figure 5A.

Table 1. The peak intensities quantified in the CO_2 -TPD patterns.

Samples	Temperature at Maximum (°C)	Quantity (cm^3/g STP)
PL-12h	119	31.7
	306	3.38
HL-12h	109	24.6
	241	29.0

A DFT calculation was performed to optimize the bulk structures of both $\text{La}_2\text{O}_2\text{CO}_3$ phases (Figure 6). The lattice constant of $\text{La}_2\text{O}_2\text{CO}_3$ in the disordered hexagonal structure was predicted by considering the ratio (c/a) of lattice parameters (a and c) of the hexagonal structure [33]. Our DFT calculated lattice constants of $\text{La}_2\text{O}_2\text{CO}_3$ nanoparticles in both monoclinic and hexagonal structures, similar to the available experimental data from the literature, which are shown in Table 2 [34,35]. On the basis of the DFT calculation, we can optimize the hexagonal type II and monoclinic type Ia $\text{La}_2\text{O}_2\text{CO}_3$ nanoparticles, as shown in Figure 7. From the optimized structure of each phase, the La atom is determined to have seven and eight oxygen atoms as nearest neighbors in monoclinic and hexagonal structures, respectively. The eight coordination numbers of the La atom in the hexagonal type II $\text{La}_2\text{O}_2\text{CO}_3$ nanoparticles can produce stronger bonding with carbonate species, which results in the higher stability of the hexagonal type II structure compared to that of the monoclinic type Ia $\text{La}_2\text{O}_2\text{CO}_3$.

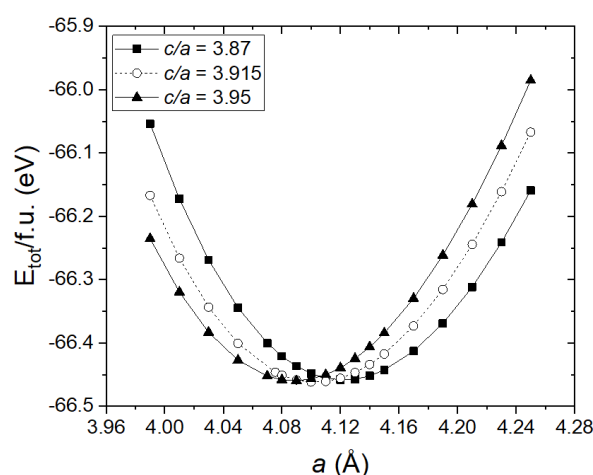


Figure 6. Density functional theory (DFT) total energy (per formula unit) of $\text{La}_2\text{O}_2\text{CO}_3$ in the hexagonal structure for three c/a values.

Table 2. Lattice constants of $\text{La}_2\text{O}_2\text{CO}_3$ in monoclinic and hexagonal structures. The experimental lattice data of monoclinic [34] and hexagonal [35] structures are available from the literature.

$\text{La}_2\text{O}_2\text{CO}_3$	DFT Calculated Data	Experimental Data [33,34]
Monoclinic	$a = 12.286 \text{ \AA}$ $b = 7.097 \text{ \AA}$ $c = 16.531 \text{ \AA}$ $\beta = 75.677$	$a = 12.239 \text{ \AA}$ $b = 7.067 \text{ \AA}$ $c = 16.465 \text{ \AA}$ $\beta = 75.690$
Hexagonal	$a = 4.100 \text{ \AA}$ $b = 4.100 \text{ \AA}$ $c = 16.053 \text{ \AA}$ $\gamma = 120$	$a = 4.076 \text{ \AA}$ $b = 4.076 \text{ \AA}$ $c = 16.465 \text{ \AA}$ $\gamma = 120$

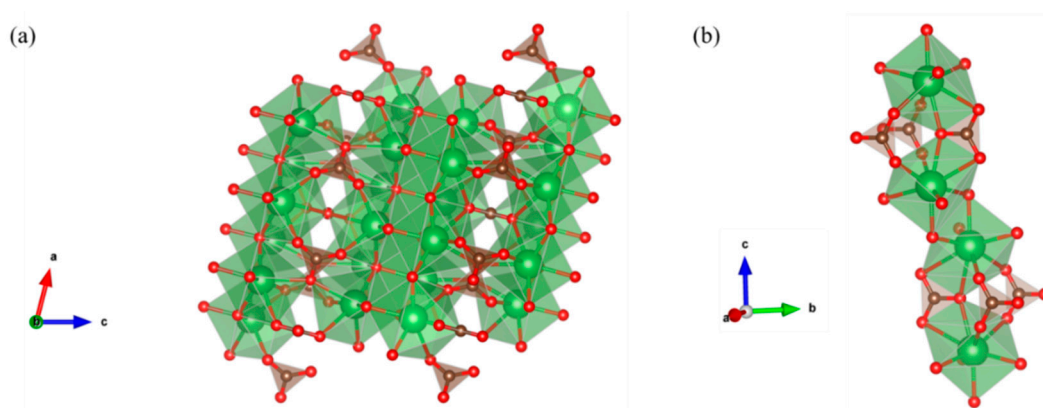


Figure 7. DFT-optimized structure of $\text{La}_2\text{O}_2\text{CO}_3$ in (a) monoclinic and (b) hexagonal phases.

3.3. CO_2 Electrochemical Reduction

Figure 8 shows LSV curves ranging from 0 to -0.6 V vs. Ag/AgCl for PL-12h and HL-12h in CO_2 -saturated 0.1 M NaHCO_3 electrolyte. HL-12h exhibits a maximum total current density of $-25.2 \text{ mA}/\text{cm}^2$ at -1.26 V vs. Ag/AgCl , whereas a maximum current density of $-17.97 \text{ mA}/\text{cm}^2$ for PL-12h is achieved at -1.438 V vs. Ag/AgCl . In addition, HL-12h shows a more positive onset potential toward CO_2 electrochemical reduction than PL-12h in Figure 8. Both the higher current density and more positive onset potential apparently indicate a higher activity toward the CO_2 electrochemical reduction in HL-12h compared to that of PL-12h.

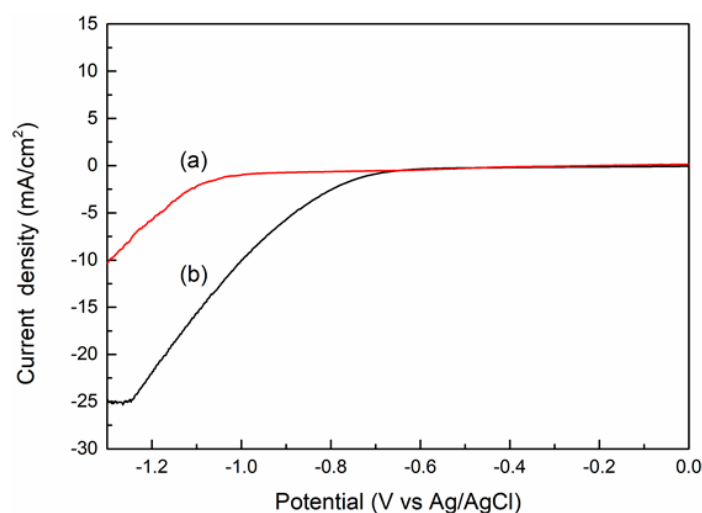


Figure 8. Linear sweeping voltammetry (LSV) curves of electrodes at various reaction times in a 0.1M NaHCO₃ solution at a scan rate of 20 mV/s: (a) PL-12h; (b) HL-12h.

The chronoamperometry (CA) experiments were performed at different potentials for each 10 min, and gaseous products were determined by GC. For both PL-12h and HL-12h, the main gaseous products are CH₄, C₂H₄, C₂H₆ and H₂. Figure 9 shows the Faraday efficiency (FE) of carbon-containing products for PL-12h and HL-12h, resulting in a much higher FE for HL-12h than those for PL-12h. C₂H₄ is a dominant carbonaceous product at lower potential. A maximum of the ethene FE (9.4%) for HL-12h is achieved at −0.6 V (vs. Ag/AgCl), while that for PL-12h is lower than 5%. Interestingly, CO gas was not detected in the potential range, even for the two La₂O₂CO₃ samples. This indicates that La₂O₂CO₃ catalysts are efficient for C-C coupling rather than desorption to form CO gas, since CO is an intermediate for CO₂ transformation to ethene during CO₂ reduction [36]. The superior electrocatalytic activity of HL-12h to PL-12h would result from the better CO₂ adsorption ability which can optimize the first step involving electron and proton transfer to form a *COOH intermediate, which is then converted to other carbonaceous products [37]. The higher electronegativity of hexagonal La₂O₂CO₃ of HL-12h leads to the better CO₂ adsorption ability [38].

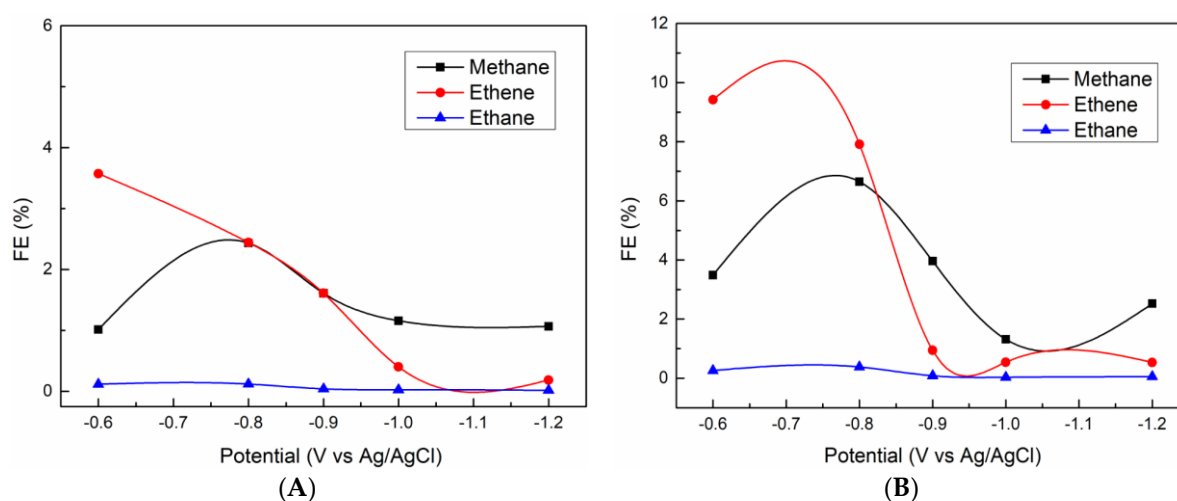


Figure 9. FE values for the (A) PL-12h and (B) HL-12h as a function of the potential.

4. Conclusions

In this study, $\text{La}_2\text{O}_2\text{CO}_3$ nanoparticles with hexagonal and monoclinic phases were prepared by different preparation methods, and the CO_2 behavior on each crystalline structure was investigated by CO_2 -TPD, TGA measurements, and CO_2 electrochemical reduction. The hydrothermal method produced the hexagonal type II $\text{La}_2\text{O}_2\text{CO}_3$ phase, whereas the monoclinic type Ia phase was synthesized by the precipitation method (PL-12h and PL-24h). The initial $\text{La}(\text{OH})_3$ phase was transformed into the $\text{La}(\text{OH})\text{CO}_3$ phase by the reaction with CO_2 supplied from air in the precipitation method. The hexagonal $\text{La}_2\text{O}_2\text{CO}_3$ phase showed a higher CO_2 adsorption ability on the surface and a higher stability in the bulk structure than the monoclinic phase, owing to the differences in optimized crystalline structures predicted by the DFT calculation. Consequently, the hexagonal $\text{La}_2\text{O}_2\text{CO}_3$ phase of HL-12h had a higher current density and a more positive onset potential than the monoclinic $\text{La}_2\text{O}_2\text{CO}_3$ of PL-12h in CO_2 electrochemical reduction.

Author Contributions: H.Y. performed the experiments and wrote the paper; K.J., S.G.K. and Y.M. contributed data analysis; E.W.S. supervised the work and polished the paper. All authors have read and agreed to the published version of the manuscript.

Funding: This research was supported by the National Research Foundation of Korea (NRF) grant funded by the Korea government (MSIT) (No. 2018R1A2B6004219 and No. 2020R1A4A4079954).

Conflicts of Interest: The authors declare no conflict of interest.

References

1. Ding, D.; Lu, W.; Xiong, Y.; Pan, X.; Zhang, J.; Ling, C.; Du, Y.; Xue, Q. Facile synthesis of $\text{La}_2\text{O}_2\text{CO}_3$ nanoparticle films and its CO_2 sensing properties and mechanisms. *Appl. Surf. Sci.* **2017**, *426*, 725–733. [[CrossRef](#)]
2. Wang, F.; Zhang, Z.; Wei, X.; Fang, Q.; Jiang, X. The shape effect of $\text{La}_2\text{O}_2\text{CO}_3$ in $\text{Pd}/\text{La}_2\text{O}_2\text{CO}_3$ catalyst for selective hydrogenation of cinnamaldehyde. *Appl. Catal. A Gen.* **2017**, *543*, 196–200. [[CrossRef](#)]
3. Li, X.; Li, D.; Tian, H.; Zeng, L.; Zhao, J.W.; Gong, J. Dry reforming of methane over $\text{Ni}/\text{La}_2\text{O}_3$ nanorod catalysts with stabilized Ni nanoparticles. *Appl. Catal. B Environ.* **2017**, *202*, 683–694. [[CrossRef](#)]
4. Park, C.Y.; Nguyen, P.H.; Shin, E.W. Glycerol carbonation with CO_2 and $\text{La}_2\text{O}_2\text{CO}_3/\text{ZnO}$ catalysts prepared by two different methods: Preferred reaction route depending on crystalline structure. *Mol. Catal.* **2017**, *435*, 99–109. [[CrossRef](#)]
5. Bosch, C.E.; Copley, M.P.; Eralp, T.; Bilbé, E.; Thybaut, J.W.; Marin, G.B.; Collier, P. Tailoring the physical and catalytic properties of lanthanum oxycarbonate nanoparticles. *Appl. Catal. A Gen.* **2017**, *536*, 104–112. [[CrossRef](#)]
6. Mu, Q.; Wang, Y. Synthesis, characterization, shape-preserved transformation, and optical properties of $\text{La}(\text{OH})_3$, $\text{La}_2\text{O}_2\text{CO}_3$, and La_2O_3 nanorods. *J. Alloys Compd.* **2011**, *509*, 396–401. [[CrossRef](#)]
7. Sun, C.; Sun, J.; Xiao, G.; Zhang, H.; Qiu, X.; Li, H.; Chen, L. Mesoscale organization of nearly monodisperse flowerlike ceria microspheres. *J. Phys. Chem. B* **2006**, *110*, 13445–13452. [[CrossRef](#)] [[PubMed](#)]
8. Yi, G.; Lu, H.; Zhao, S.; Ge, Y.; Yang, W. Synthesis, characterization, and biological application of size-controlled nanocrystalline $\text{NaYF}_4: \text{Yb}, \text{Er}$ phosphors. *Nano Lett.* **2004**, *4*, 2191–2196. [[CrossRef](#)]
9. Li, G.; Peng, C.; Zhang, C.; Xu, Z.; Shang, M.; Yang, D.; Kang, X.; Wang, W.; Li, C.; Cheng, Z.; et al. $\text{Eu}^{3+}/\text{Tb}^{3+}$ -Doped $\text{La}_2\text{O}_2\text{CO}_3/\text{La}_2\text{O}_3$ nano/microcrystals with multiform morphologies: Facile synthesis, growth mechanism, and luminescence properties. *Inorg. Chem.* **2010**, *49*, 10522–10535. [[CrossRef](#)]
10. Lin, J. Multiform oxide optical materials via the versatile pechini-type sol-gel process. *Proc. Int. Meet. Inf. Disp.* **2008**, *8*, 1247–1250. [[CrossRef](#)]
11. Van Le, T.; Che, M.; Kermarec, M.; Louis, C.; Tatibouët, J.M. Structure sensitivity of the catalytic oxidative coupling of methane on lanthanum oxide. *Catal. Lett.* **1990**, *6*, 395–400. [[CrossRef](#)]
12. Wang, F.; Ta, N.; Li, Y.; Shen, W. $\text{La}(\text{OH})_3$ and $\text{La}_2\text{O}_2\text{CO}_3$ nanorod catalysts for Claisen-Schmidt condensation. *Chin. J. Catal.* **2014**, *35*, 437–443. [[CrossRef](#)]
13. Lacombe, S.; Geantet, C.; Mirodatos, C. Oxidative coupling of methane over lanthana catalysts. I. Identification and role of specific active-sites. *J. Catal.* **1995**, *151*, 439–452. [[CrossRef](#)]

14. Chen, H.; Yu, H.; Peng, F.; Wang, H.; Yang, J.; Pan, M. Efficient and stable oxidative steam reforming of ethanol for hydrogen production: Effect of in situ dispersion of Ir over Ir/La₂O₃. *J. Catal.* **2010**, *269*, 281–290. [[CrossRef](#)]
15. Wang, H.; Fang, Y.; Liu, Y.; Bai, X. Perovskite LaFeO₃ supported bi-metal catalyst for syngas methanation. *J. Nat. Gas Chem.* **2012**, *21*, 745–752. [[CrossRef](#)]
16. Turcotte, R.P.; Sawyer, J.O.; Eyring, L. On the rare earth dioxymonocarbonates and their decomposition. *Inorg. Chem.* **1969**, *8*, 238–246. [[CrossRef](#)]
17. Olafsen, A.; Fjellvåg, H. Synthesis of rare earth oxide carbonates and thermal stability of Nd₂O₂CO₃ II. *J. Mater. Chem.* **1999**, *9*, 2697–2702. [[CrossRef](#)]
18. Hirsch, O.; Kvashnina, K.O.; Luo, L.; Süess, M.J.; Glatzel, P.; Koziej, D. High-energy resolution X-ray absorption and emission spectroscopy reveals insight into unique selectivity of La-based nanoparticles for CO₂. *Proc. Natl. Acad. Sci. USA* **2015**, *112*, 15803–15808. [[CrossRef](#)]
19. Hölsä, J.; Turkki, T. Preparation, thermal stability and luminescence properties of selected rare earth oxycarbonates. *Thermochim. Acta* **1991**, *190*, 335–343. [[CrossRef](#)]
20. Koyabu, K.; Masui, T.; Tamura, S.; Imanaka, N. Synthesis of a new phosphor based on rare earth oxycarbonate. *J. Alloys Compd.* **2006**, *408–412*, 867–870. [[CrossRef](#)]
21. Yu, H.; Men, Y.; Shin, E.W. Structural properties of disordered macroporous La₂O₂CO₃/ZnO materials prepared by a solution combustion method. *Korean J. Chem. Eng.* **2019**, *36*, 522–528. [[CrossRef](#)]
22. Kresse, G.; Furthmüller, J. Efficient iterative schemes for ab initio total-energy calculations using a plane-wave basis set. *Phys. Rev. B* **1996**, *54*, 11169–11186. [[CrossRef](#)] [[PubMed](#)]
23. Kresse, G.; Furthmüller, J. Efficiency of ab-initio total energy calculations for metals and semiconductors using a plane-wave basis set. *Comput. Mater. Sci.* **1996**, *6*, 15–50. [[CrossRef](#)]
24. Perdew, J.P.; Burke, K.; Ernzerhof, M. Generalized gradient approximation made simple. *Phys. Rev. Lett.* **1996**, *77*, 3865–3868. [[CrossRef](#)] [[PubMed](#)]
25. Monkhorst, H.J.; Pack, J.D. Special points for Brillouin-zone integrations. *Phys. Rev. B* **1976**, *13*, 5188–5192. [[CrossRef](#)]
26. Hou, Y.H.; Han, W.C.; Xia, W.S.; Wan, H.L. Structure sensitivity of La₂O₂CO₃ catalysts in the oxidative coupling of methane. *ACS Catal.* **2015**, *5*, 1663–1674. [[CrossRef](#)]
27. Fleming, P.; Farrell, R.A.; Holmes, J.D.; Morris, M.A. The rapid formation of La(OH)₃ from La₂O₃ powders on exposure to water vapor. *J. Am. Ceram. Soc.* **2010**, *93*, 1187–1194. [[CrossRef](#)]
28. Fedorov, P.P.; Nazarkin, M.V.; Zakalyukin, R.M. On polymorphism and morphotropism of rare earth sesquioxides. *Crystallogr. Rep.* **2002**, *47*, 281–286. [[CrossRef](#)]
29. Bakiz, B.; Guinneton, F.; Arab, M.; Benhachenu, A.; Gavarria, J.-R. Elaboration, characterization of LaOHCO₃, La₂O₂CO₃ and La₂O₃ phases and their gas solid interactions with CH₄ and CO gases. *Moroc. J. Condens. Matter Soc.* **2010**, *12*, 60–67.
30. Rémiás, R.; Kukovecz, Á.; Darányi, M.; Kozma, G.; Varga, S.; Kónya, Z.; Kiricsi, I. Synthesis of zinc glycerolate microstacks from a ZnO nanorod sacrificial template. *Eur. J. Inorg. Chem.* **2009**, *2009*, 3622–3627. [[CrossRef](#)]
31. Manoilova, O.V.; Podkolzin, S.G.; Tope, B.; Lercher, J.; Stangland, E.E.; Goupil, J.M.; Weckhuysen, B.M. Surface acidity and basicity of La₂O₃, LaOCl, and LaCl₃ characterized by IR spectroscopy, TPD, and DFT calculations. *J. Phys. Chem. B* **2004**, *108*, 15770–15781. [[CrossRef](#)]
32. Di Cosimo, J.I.; Díez, V.K.; Xu, M.; Iglesia, E.; Apesteguía, C.R. Structure and surface and catalytic properties of Mg-Al basic oxides. *J. Catal.* **1998**, *178*, 499–510. [[CrossRef](#)]
33. Sholl, D.S.; Steckel, J.A. *Density Functional Theory: A Practical Introduction*; John Wiley & Sons, Inc.: Hoboken, NJ, USA, 2009.
34. Olafsen, A.; Larsson, A.K.; Fjellvåg, H.; Hauback, B.C. On the crystal structure of Ln₂O₂CO₃ II (Ln = La and Nd). *J. Solid State Chem.* **2001**, *158*, 14–24. [[CrossRef](#)]
35. Atfield, J.P. Structure determinations of La₂O₂CO₃-II and the unusual disordered phase La₂O_{2.52}(CO₃)_{0.74} Li_{0.52} using powder diffraction. *J. Solid State Chem.* **1989**, *82*, 132–138. [[CrossRef](#)]
36. Zhang, B.; Zhang, J.; Hua, M.; Wan, Q.; Su, Z.; Tan, X.; Liu, L.; Zhang, F.; Chen, G.; Tan, D.; et al. Highly electrocatalytic ethylene production from CO₂ on nanodeficient Cu nanosheets. *J. Am. Chem. Soc.* **2020**, *142*, 13606–13613. [[CrossRef](#)] [[PubMed](#)]

37. Zhang, J.; Yin, R.; Shao, Q.; Zhu, T.; Huang, X. Oxygen vacancies in amorphous InO_x nanoribbons enhance CO₂ adsorption and activation for CO₂ electroreduction. *Angew. Chem. Int. Ed.* **2019**, *58*, 5609–5613. [[CrossRef](#)] [[PubMed](#)]
38. Horiuchi, T.; Hidaka, H.; Fukui, T.; Kubo, Y.; Horio, M.; Suzuki, K.; Mori, T. Effect of added basic metal oxides on CO₂ adsorption on alumina at elevated temperatures. *Appl. Catal. A Gen.* **1998**, *167*, 195–202. [[CrossRef](#)]

Publisher’s Note: MDPI stays neutral with regard to jurisdictional claims in published maps and institutional affiliations.



© 2020 by the authors. Licensee MDPI, Basel, Switzerland. This article is an open access article distributed under the terms and conditions of the Creative Commons Attribution (CC BY) license (<http://creativecommons.org/licenses/by/4.0/>).